Semiconductor strain engineering in a driven optomechanical oscillator

Thesis by
Tommaso Raimondi

Double Master of Science in
Nanotechnologies and Quantum Devices (NanoQuad)

POLITECNICO DI TORINO - UNIVERSITÉ PARIS CITÉ
ÉCOLE NORMALE SUPÉRIEURE

Supervisors

prof. Carlo Sirtori	École Normale Supérieure
prof. Yanko Todorov	École Normale Supérieure
prof. Carlo Ricciardi	Politecnico di Torino
prof. Maria Luisa della Rocca	Université Paris Cité

Paris, France

2023
Defended 30/06/2023

TABLE OF CONTENTS

Chapter 1

INTRODUCTION

The main goal of the project is to give the proof of concept of the use of optomechanical oscillators to induce appreciable amount of strain in semiconductors. The possibility to engineer the strain in semiconductors has the purpose of changing their optical properties for future applications, such as tuning lasers emissions via the modification of the bandstructure.
The key concept of this work relies on the connection between classical and quantum phenomena, indeed the strain in the oscillator is controlled through the application of an external potential which has the effect of making the sample oscillate according to the laws of classical mechanics. The result is the ability to tune through an external input the optical properties of the semiconductor, such as the transitions of the photons inside the material and the refractive index. The transduction mechanism that drives the sample is based on the dielectric force experienced by a polarizable material immersed in an inhomogeneous electric field, in fact the sample is fabricated to enable the application of an external signal which makes the beam move toward the maximum of the field due to the generated electric field gradient. In a perfectly symmetric sample the gradient would only be in the out-of-plane direction, anyway since the electrodes are not symmetrically separated due to imperfect fabrication, there is a partial influence of the drive on the in-plane mode.

The research project is entirely carried out at the Quantum physics and devices (QUAD) group at the Laboratoire de Physique de l'Ecole Normale Supérieure (LPENS). The team aims to develop high-level research with technological and application content. The activities exploit the concepts of quantum mechanics, in particular in the field of light-matter interaction, to realize new opto-electronic devices. The main objective is the understanding and control of new quantum phenomena in materials of reduced dimensionality and suitable for "top-down" clean room manufacturing (semiconductors, 2D materials, metals and other materials related to nanotechnological processes). The devices realized are in the infrared (3-300 μm) and microwave range, portions of the electromagnetic spectrum with a high potential for applications and technology transfer. The work is organized in 3 directions – N-body quantum physics – Plasmonics and metamaterials – Photonics and infrared devices. The team is supported by an ENS-THALES Industrial Chair.

1.1 Sample description

The oscillator used has the same fabrication parameters of the one used in a previous research project of the group (Liu et al., 2022). The device is designed in a dog-bone shape which consists in two anchoring pillars and a suspended doubly clumped beam of length $l = 17\,\mu m$ and width $w = 250\,nm$. The structure is a bilayer made of Au (thickness $\mu_{Au} = 150\,nm$) on top of GaAs (thickness $\mu_{GaAs} = 200\ nm$) so the total thickness is $\mu = 350\,nm$, the presence of Au is due to the previous research aim of the group in which Au worked as receiving antenna that resonantly absorbed THz radiation. In figure 1.1 are reported a scheme and a Scanning Electron Microscope (SEM) image of the sample. The electrodes on the sides of the oscillator can generate an electric field represented in blue which is able to polarize the bridge and in the case of perfectly symmetric structure push it only out-of-plane due to the gradient of the electric field in that direction. From the geometrical parameters of the bridge is possible to calculate the two expected fundamental flexural mode frequencies, since the width is lower than the thickness, the in-plane mode should have a resonant frequency lower with respect to the out-of-plane mode, respectively around $2.4\,MHz$ and $3.37\,MHz$. It has been proved in the past that the fabrication can generate built-in stress in the bridge causing a significant shift of the resonant frequencies, and in this work is explained why it is believed that the order of the in-plane and out-of-plane modes is inverted. Indeed, based on previous results (Liu et al., 2022) the beam is expected to have a mode around $3\,MHz$ and the other mode around $3.5\,MHz$, and they are respectively considered as the out-of-plane mode and the in-plane mode. The explanation regarding the individuation of the in-plane and out-of-plane mode is presented later at the end of the second chapter for the sake of clarity.

Finally, since the sample is composed by Au and GaAs layers, is necessary to calculate an average density $\rho = \frac{\rho_{Au} \cdot \mu_{Au} + \rho_{GaAs} \cdot \mu_{GaAs}}{\mu_{Au} + \mu_{GaAs}} \sim 11.3 \cdot 10^3\ kg/m^3$ that enable us to threat the beam as a unique element.

In table 1.1 are summarized all the key properties of the sample.

density ρ	$11.3 \cdot 10^3\ kg/m^3$
length l	$17\ \mu m$
width w	$250\ nm$
thickness μ	$350\ nm$

Table 1.1: Sample properties.

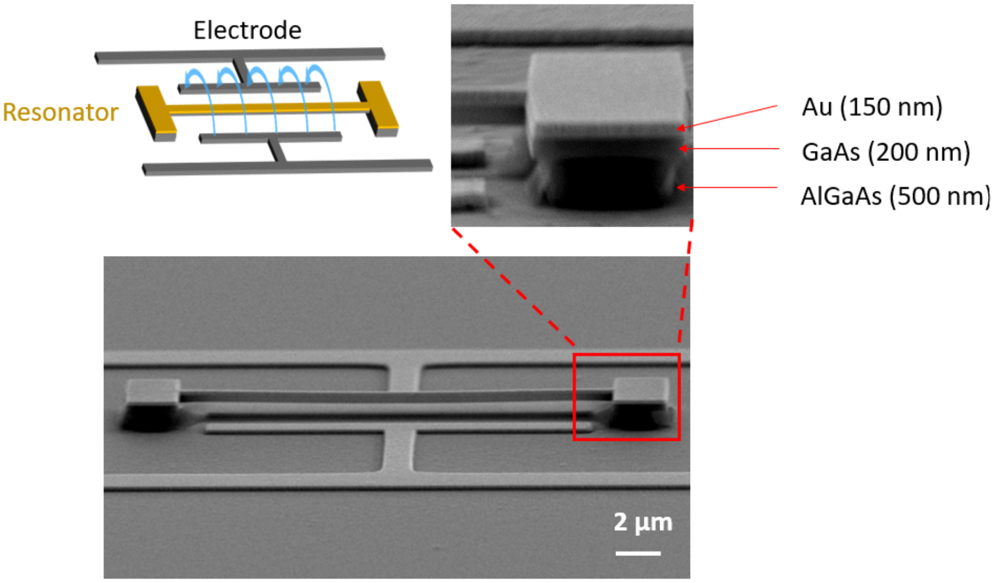

Figure 1.1: Scheme and SEM image of Doubly clumped beam made of Au and GaAs.

1.2 The beam as an harmonic oscillator

In order to describe the physics of the experiment in a simple way, the beam is treated as a one dimensional harmonic oscillator. Since the length of the beam is much larger than the width and the thickness, the equation of motion of the beam can be described by the Euler-Bernoulli equation (Senturia, 2001), which gives multiple angular frequency solutions called eigenmodes Ω_n.

Furthermore it is possible to use the spring model in which there is a one to one correspondence between each angular eigenfrequency Ω_n and an equivalent harmonic oscillator with the same frequency. The equivalent harmonic oscillator, apart from having the same vibrational frequency, has corresponding values of effective mass m_{eff} and effective stiffness k_{eff} different with respect to the real mass of the beam m_0 and real stiffness k_0. As explained in the detail in the doctoral thesis Calabrese, 2019, by equating the kinetic energy of one oscillation mode Ω_n and the energy of an harmonic oscillator with frequency Ω_n it is possible to obtain a relation between m_{eff} and the real mass of the beam m_0. In the case of this study since we are dealing with the first order mode of a doubly clumped beam, which reaches maximum displacement amplitude in the middle, the relation between the effective mass and the real mass for the first order flexural mode will be the following: $\frac{m_{eff}}{m_0} \sim 0.4$.

The procedure to get the effective stiffness k_{eff} follows the same principle mapping the elastic potential energy associated to the eigenmode Ω_n into the potential energy of a one-dimensional harmonic oscillator of frequency Ω_n (Calabrese, 2019). The effective stiffness will be $k_{eff} = m_{eff} \cdot \Omega_n^2$, but it is also taken into account that the experimentally measured modes Ω_n will differ

from their theoretical values, so k_{eff} will be evaluated after the experimental determination of the modes Ω_n to be more accurate. From now on the bridge will be considered exactly an harmonic oscillator, so these two terms will be used equivalently. In figure 1.2 is represented the harmonic oscillator scheme used to describe the bridge, image taken from Calabrese, 2019.
Having explained the model in use it is straigthforward to compute the effective mass of the beam for the first order mode as $m_{eff} = 0.4 \cdot m_0 = 0.4 \cdot \rho \cdot l \cdot w \cdot \mu = 6.7pg$.

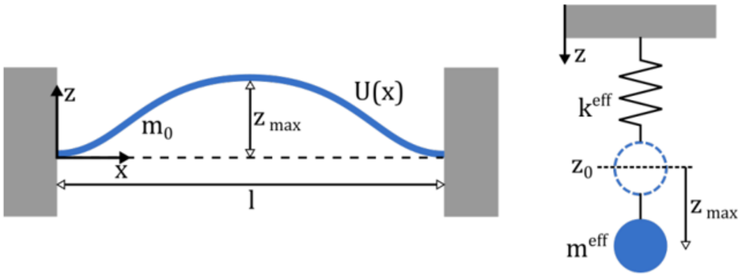

Figure 1.2: On the left the bridge of length l and mass m_0 which oscillates with displacement U(x). On the right the equivalent harmonic oscillator with effective mass m_{eff} and effective stiffness k_{eff}.

1.3 Thermal noise (Langevin force)

The harmonic oscillator model described in the previous section allows us to describe the bridge through the dynamic equation of motion of an harmonic oscillator (Aspelmeyer, Kippenberg, and Marquardt, 2014):

$$m_{eff}\frac{d^2z(t)}{dt^2} + m_{eff}\Gamma\frac{dz(t)}{dt} + m_{eff}\Omega_n^2 z(t) = F_{ext}(t) \tag{1.1}$$

where m_{eff} is the effective mass of the bridge, $z(t)$ is the amplitude of oscillation, Γ is the damping rate due to presence of non ideal dissipation mechanisms such as the air friction and F_{ext} includes any external forces applied on the oscillator. This equation contains all the possible contributions to the dynamics of the harmonic oscillator, which are the elastic behaviour that is proportional to Ω_n^2, the damping due to non ideal dissipation contained in the term proportional to Γ and the external forces in F_{ext}.
Since experimentally the dynamics of the beam is analyzed in frequency, we need to create a link between the theory and experiment writing the equation (1.1) in the domain of the angular frequency ω:

$$\begin{aligned} m_{eff}(\Omega_n^2 - \omega^2)z(\omega) + i m_{eff}\Gamma\omega z(\omega) &= F_{ext}(\omega) \\ \chi_m(\omega) = \frac{z(\omega)}{F_{ext}(\omega)} &= \frac{1}{m_{eff}[(\Omega_n^2 - \omega^2) + i\Gamma\omega]} \end{aligned} \tag{1.2}$$

where $z(\omega)$ and $F_{ext}(\omega)$ are respectively the Fourier transform of $z(t)$ and $F_{ext}(t)$ and $\chi_m(\omega)$ is the mechanical susceptibility. Even without applying any force on the oscillator, there is always an external force F_{ext} contribution due to the so called thermomechanical noise force or Langevin force that will make the oscillator vibrate. The Langevin force has zero statistical average and it is completely uncorrelated in time, it is the effect of the finite temperature T of the system at thermal equilibrium which make the harmonic oscillator perform a motion characterized by random varying amplitude and phase which is called Brownian motion (Aspelmeyer, Kippenberg, and Marquardt, 2014).

The last quantity we need to introduce is the Fourier transform of the auto-correlation of displacement called power spectral density (Aspelmeyer, Kippenberg, and Marquardt, 2014):

$$S_{zz}(\omega) = \frac{1}{2\pi}\int_{-\infty}^{\infty} \langle z(t)z(0)\rangle e^{-(i\omega t)}dt = 2\frac{k_B T}{\omega}\Im[\chi_m(\omega)] \tag{1.3}$$

The power spectral density $S_{zz}(\omega)$ is the function that describes how much power is given to the oscillator at each value of frequency. In other words the temperature of the bridge makes it vibrate at all angular frequencies ω from $-\infty$ to $+\infty$, but due to its geometrical dimensions the bridge will be mainly allowed to oscillate around its eigenmodes Ω_n found solving the Euler-Bernoulli equation. As a consequence of this, $S_{zz}(\omega)$ will assume higher values around the angular frequencies Ω_n and the more the oscillation of the bridge is selective and restricted to Ω_n with respect to the rest of the spectrum, the more the quality of the specific mode Ω_n will be higher. Further details on the concept of quality of an oscillator and its estimation are contained in the next chapter about the characterization of the device. Equation (1.3) evidences also the fluctuation-dissipation theorem which puts in relation the power spectral density $S_{zz}(\omega)$ with the imaginary part of the mechanical susceptibility $\chi_m(\omega)$ and the thermal energy $k_B T$. This relation enables to underscore that the power spectral density $S_{zz}(\omega)$ has a Lorentzian shape dependence on the angular frequency ω since its proportional to the imaginary part of the susceptibility $\Im[\chi_m(\omega)]$, see equation 1.2.

Finally the power spectral density of the displacement $S_{zz}(\omega)$ can be related to the variance of the displacement of the oscillator through the Wiener-Khinchin theorem (Aspelmeyer, Kippenberg, and Marquardt, 2014). Since the oscillator goes up and down with respect to the equilibrium position z_0, the average value of the displacement z will be zero, so the variance will coincide with the average of the squared amplitude $\langle z^2 \rangle$:

$$\int_{-\infty}^{\infty} S_{zz}(\omega)\frac{d\omega}{2\pi} = \langle z^2 \rangle \tag{1.4}$$

If experimentally we succeed to estimate the power spectral density $S_{zz}(\omega)$, then the equation (1.4) allows us to calculate the correspondent variance of the mechanical displacement $\langle z^2 \rangle$ and to connect it to the thermal energy $k_B T$ through the energy equipartition theorem (Butt and Jaschke, 1995), which states that at thermal equilibrium each degree of freedom of a system has the same average energy. In the case of an harmonic oscillator its average kinetic energy in one dimension is proportional to the temperature of the system:

$$\frac{1}{2} m_{eff} \Omega_n^2 \langle z^2 \rangle = \frac{1}{2} k_B T \tag{1.5}$$

Equation (1.5) evidences that the higher modes show smaller amplitude of oscillation, that is the reason why will deal just with the very first order mode Ω_0 of the oscillator, at a certain value of frequency the amplitude is so small that is below the level of the detection of the setup. In practice the theoretical model described in this chapter is used separately for the characterization of the out-of-plane first order mode and the in-plane first order mode of the bridge.

1.4 Experimental setup

In order to obtain an estimation of the power spectral density $S_{zz}(\omega)$ it is necessary to built a setup which is able of doing a read out of the oscillation of the bridge as function of the frequency. The setup used to characterize the sample is exactly the same used for previous research goals in the past (Calabrese, 2019), the main idea is to detect the mechanical vibration through the intensity fluctuation of a laser beam. In figure 1.3 is reported the experimental setup used for the characterization of the device, image reproduced from the PhD thesis Calabrese, 2019.

The sample is kept inside a vacuum chamber, this is to enable measurements at different values of pressure, so to compare the device behaviour under different conditions. The presence of the LED lamp is relevant to be able to have in the camera an image of the sample, this trick helps the alignment since it is possible to see where the laser is hitting the sample. Indeed it is important to try to detect the oscillation of the bridge in the middle, since the amplitude will be higher and also the corresponding signal to noise ratio. The light coming from the LED lamp is directed onto the sample by a dichroic mirror (DM) and the part of it that is reflected by the sample is than conveyed toward the camera, the resulting image is visible on the computer.

For what concerns the detection, the idea is to use a near infrared (NIR) laser with $\lambda = 910\,nm$ and focus it on top of the bridge such that the laser is parallel to the out-of-plane direction, which is the

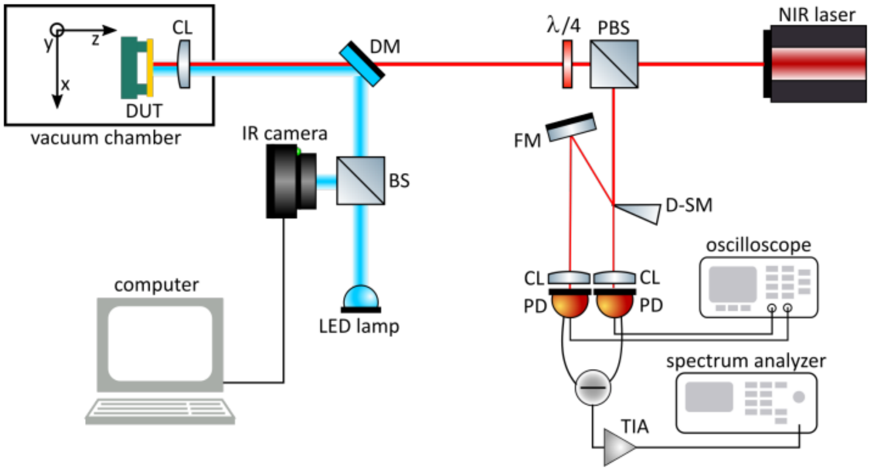

Figure 1.3: Experimental setup for measurement of thermomechanical noise of the optomechanical oscillators. Red lines indicate the optical path of the NIR laser beam, while thick nuanced blue lines represent the path of the white light from the LED lamp. BS = Beam splitter, CL = converging lens, DM = dichroic mirror, D-SM = D-shaped mirror, DUT = device under test, FM =flat mirror, PBS = polarizing beam splitter, PD = photodiode, TIA =trans-impedence amplifier.

z-axis in figure 1.3. As it happens for the white light, part of the infrared radiation is reflected by the oscillating sample, but when the laser light comes back it passes for the second time through a $\lambda/4$ waveplate which maximizes the amount of light that is directed along the x-axis by a polarizing beam splitter (PBS). As a result, the light containing the information about the oscillation of the sample is now directed toward the x-axis where it encounters a D-shaped mirror (D-SM) that enables the implementation of the knife-edge technique (Karabacak et al., 2006). The knife-edge technique consists on aligning the D-SM in such a way that part of the light beam is untouched and directly goes into one photodiode (PD) and the rest is instead reflected toward a flat mirror (FM) which sends the light to another photodiode. Before each photodiode there is a correspondent converning lens (CL) which is needed to focus the laser into the detector, both the PDs are integrated into one balanced photodetection unit (Thorlabs $PDB110A$) which gives as output the difference between the diodes photocurrents. Actually what is finally sent to the spectrum analyser is the photocurrents difference after being converted into voltage by a trans-impedence amplifier (TIA). The result of this scheme is to have a balanced detection which enables to maximize the signal to noise ratio because of the subtraction between the dark-current noises of the two PDs. Furthermore the implementation of the knife-edge technique allows the detection of the in-plane oscillation (x-y plane). In fact the spot of light on the D-shaped mirror oscillates at the in-plane frequency and the light is continuosly distributed differently between the two photodiodes, which means that the balanced photodiode receives also a signal at the frequency of the in-plane oscillation. The out-of-plane oscillation frequency is instead always contained in the laser light after reflection,

because the up and down movement of the bridge causes interference between the incident and reflected laser light.
In the figure 1.4, reproduced from Calabrese, 2019, are schematized the different read-out mechanisms of detection for the out-of plane and in-plane oscillation.

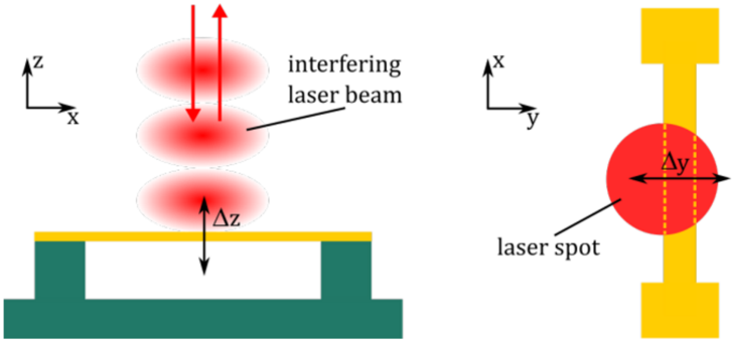

Figure 1.4: On the left the interfering between the impinging and reflected laser due to out-of-plane oscillation. On the right the influence of in-plane oscillation changes the area probed by the laser spot.

The effects described in figure 1.4 cause variations of the intensity of the laser which occur at the frequency of each of the eigenmodes, so the spectrum analyzer is able to register this variation of intensity and to display the voltage output of the balanced photodiode as function of the frequency. In other words the spectrum analyzer is able to reconstruct the voltage power spectral density of the system $S_{vv}(\omega)$, then the voltage signal must be related to the amplitude in order to obtain the amplitude power spectral density $S_{zz}(\omega)$.

Technical insights on the setup

In this subsection there is a comment on technicalities about how to handle the setup as instructions for future work in the research group, these insights come from the experience acquired during the characterization of the device.
First of all in figure 1.4 is not present a diaphragm which is in front of the NIR laser, this diaphragm is very important to be able to see the Brownian motion on the spectrum analyser. The reason for which the presence of the diaphragm is of relevance is because it gives to the laser spot a better shape. It is clearly visible in the camera that the diaphragm must be opened enough to have a good amount of light impinging on the sample and so enough signal, but at the same time it must not be opened too much otherwise the background noise covers the Brownian motion signal. This effect is probably enhanced by the fact that the spot of the laser is bigger than the bridge size.
Furthermore, the converging lens in front of the device focuses differently the light coming from the LED lamp and the light of laser, so while aligning the system a good compromise between

seeing well the sample and trying to effectively focus the laser must be found. When the Brownian motion starts to be visible above the noise in the spectrum analyser than it is good to change the focus in order to maximize the result.

Finally the position of the D-shaped mirror is able to determine if we maximize the detection of the out-of-plane or the in-plane mode, so it must be touched with caution to better see the two modes as desired.

Last but not least, the amount of signal coming from both the photodiodes can be checked on the oscilloscope, which displays the DC voltage coming from each diode. The goal is to try to have equal signals on the oscilloscope such that the dark noise coming from the diodes can be canceled, anyway the maximum signal to noise ratio in the spectrum analyser can be obtained even without having exactly the same output from the two detectors.

Chapter 2

DEVICE CHARACTERIZATION

The characterization of the device starts with the determination of the quality factor of each of the two first order eigenmodes. The quality factor is a measure of how much the oscillator is able to selectively vibrate only at its eigenfrequency with respect to the rest of the frequency spectrum. Two different methods to obtain an estimation of the quality factor are implemented and compared in the following section 2.1 of this chapter. Then in section 2.2 are discussed the limits at which the device can be driven using the external RF voltage, the non-linear oscillation effects are taken into account to understand which is the maximum obtainable amplitude of oscillation.

2.1 Quality factor

As said in the previous chapter the power spectral density $S_{zz}(\omega)$ has a Lorentzian shape dependence on the angular frequency ω, and so the quality factor Q is straightforward defined as in the following formula:

$$Q = \frac{\Omega_0}{\Delta\Omega} \tag{2.1}$$

In this formula Ω_0 is again the angular eigenfrequency of the mode under consideration and $\Delta\Omega$ is simply the full width half maximum of the power spectral density which is a Lorentzian curve.

Spectrum analyser method

The first method of the determination of the quality factors Q of the two modes is implementing the exact same scheme described in the figure 1.3. The output of the balanced photodetection unit is represented by the spectrum analyser in power decibel dB, then the acquisition is converted in volt V, squared and finally divided by the resolution bandwidth (RBW) of the instrument to get the voltage power spectral density. The resolution bandwidth RBW is the inverse of the integration time for each point plotted by the spectrum analyser, so it must be chosen to have a good integration but such that the measurement is not too long. Calling y the data acquired in dB the corresponding value of voltage power spectral density in V^2/Hz is obtained through the following formula:

$$S_{vv}(\omega) = \frac{10^{(y/10)}}{RBW} \tag{2.2}$$

The very first measurements are performed with the sample held at ambient pressure (1 atm), after converting the data to power spectral density the result is fitted by a curve which is a Lorentzian plus a constant, this is because we have to consider that the spectrum analyser is actually detecting the power spectral density due to the sample oscillation plus a superimposed constant level of noise coming from the rest of the system. Indeed in any of the following fits of the spectrum analyser method the fitting function is as in this equation:

$$y(x) = c + \frac{a}{(x - f_0)^2 + \frac{d^2}{4}} \tag{2.3}$$

Equation (2.3) is a Lorentzian function plus a constant c, where x is the variable corresponding to the frequency axis and all the other letters are free parameters of the fit.

It is presented in figure 2.1 an acquisition taken with the spectrum analyser of both the out-of plane and the in-plane mode at ambient pressure.
As we can see, it is already visible that the eigenfrequencies are close to the expected values of 3 MHz for the out-of-plane mode and 3.5 MHz for the in-plane mode. The spectrum is a superposition of the Lorentzian curves due to the oscillation of the bridge at the modes frequencies with a noise floor.
Moreover in this figure there is an important technical information which is that the in-plane mode (around 3.6 MHz) is higher with respect to the out-of-plane mode, this is due to the obtained alignment of the optical system, in particular to the position of the D-shape mirror.

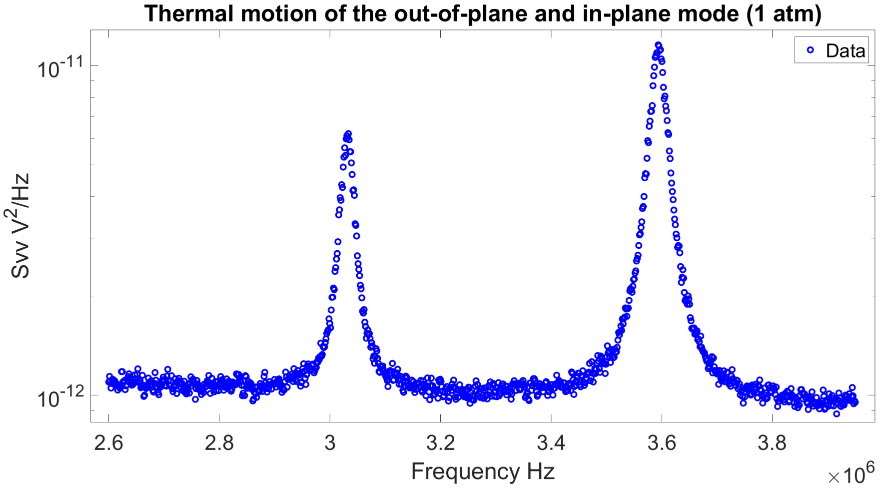

Figure 2.1: Spectrum analyser acquisition of both the out-of-plane and the in-plane mode at ambient pressure (1 atm). Measure taken with RBW = 13000 Hz. The empty blue dots are the voltage power spectral density coming from the data converted with the equation (2.2), the plot is in logaritmic scale on the y-axis.

For what concerns the single mode characterization, to have a good fit it is very important to zoom with the spectrum analyser into one peak per time, this means reducing the span of the frequency around the analyzed peak of oscillation. Furthermore with a smaller span the resolution bandwidth RBW can be reduced to favour a better estimation of the Lorentizan shape. In the figure 2.2 there are the results of the characterization of each single mode at 1 atm and at $4.1 \cdot 10^{-1} mbar$, for convenience we will call vacuum this last value of pressure.
Here and in all the succeeding plots of this section, the x-axis is the frequency expressed in Hz, indeed the correspondent found eigenfrequency is called f_0, see that the angular eigenfrequency Ω_0 is $\Omega_0 = 2\pi f_0$.

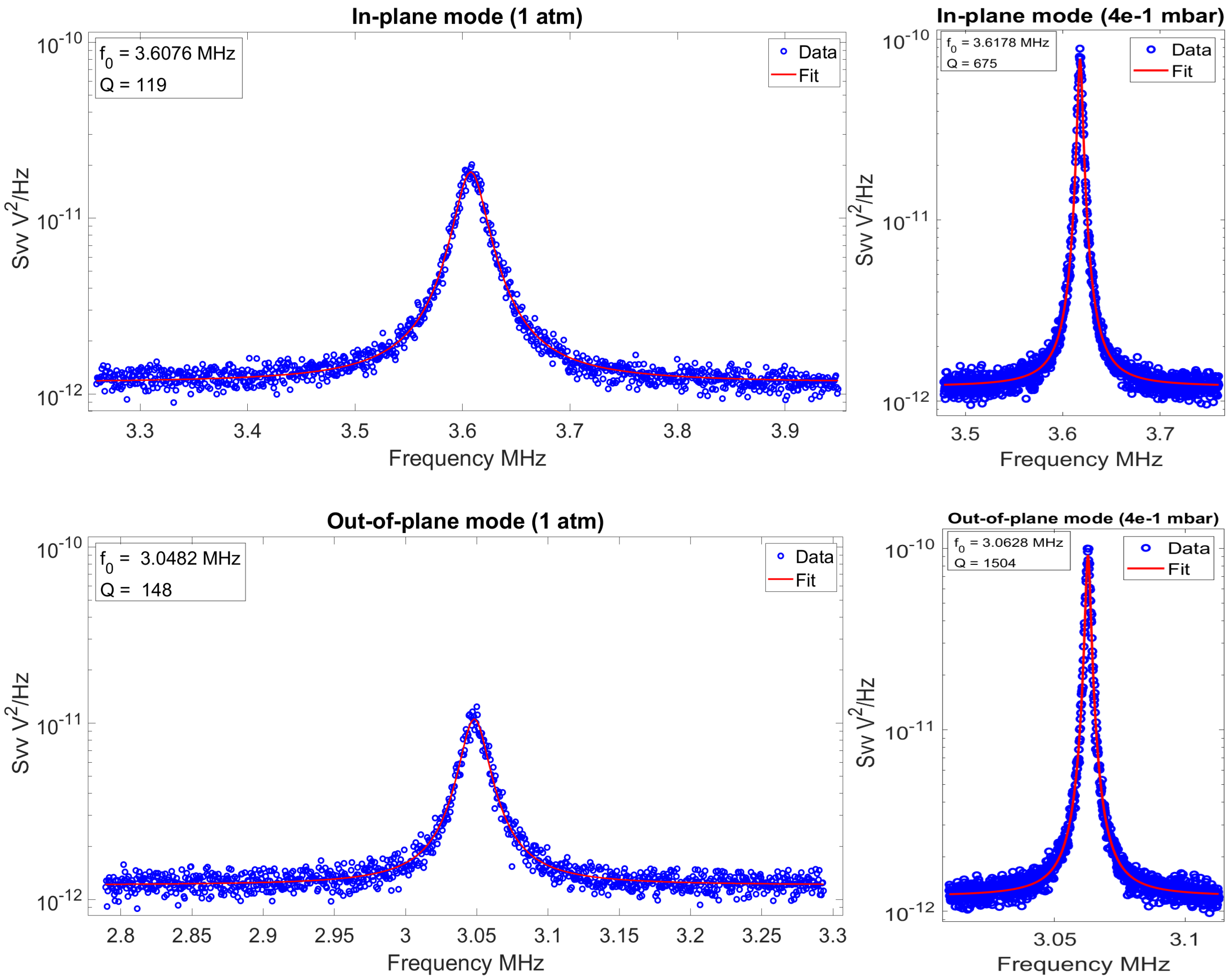

Figure 2.2: Brownian motion at ambient pressure (1 atm) and in vacuum ($4.1 \cdot 10^{-1} mbar$) of the in-plane mode and out-of-plane mode. The resolution bandwidth of all the measures is RBW=100 Hz. The empty blue dots are the voltage power spectral density coming from the data converted with the equation (2.2), while the red curve is the fit performed with the function (2.3), the plot is in logaritmic scale on the y-axis. In the upper left of each plot are reported the values of the obtained eigenfrequency f_0 and the quality factor Q.

In the table 2.1 are summarized the results extracted by the Lorentzian fit of the thermal motion at ambient pressure and in vacuum, coherently in both cases the quality factor is higher for the out-of plane mode with respect to the in-plane mode.

Pressure	Mode	f_0	Q
1 atm	In-plane	$3.6076\ MHz$	119
	Out-of-plane	$3.0482\ MHz$	148
vacuum	In-plane	$3.6178\ MHz$	675
	Out-of-plane	$3.0628\ MHz$	1504

Table 2.1: Quality factor Q and eigenmode f_0 of the in-plane and out-of-plane mode at ambient pressure (1 atm) and in vacuum ($4.1 \cdot 10^{-1} mbar$).

In vacuum a lower amount of particles can damp the oscillation of the bridge, so a smaller damping rate Γ is expected, which means a lower full width half maximum FWHM of the Lorentzian and therefore higher quality factors. Moreover in vacuum, not only the quality factor increases but there is a much better signal to noise ratio, so the Lorentzian peaks exit more from the noise floor with respect to the ambient pressure case, see figure 2.2. The results are coherent and the quality factor increases for both modes, but more for the out-of-plane where there is an increase of a factor ~ 10 with respect to the ambient pressure. At low pressure the eigenfrequencies show a little shift to higher values with respect to ambient pressure, this phenomenon can be explained by the fact that due to resistance of the air particles to the motion of the beam, at ambient pressure there is an higher effective mass m_{eff} which leads to a lower eigenfrequency, from the relation $\Omega_0 = \sqrt{\frac{k_{eff}}{m_{eff}}}$.

Before going on with the second method is interesting to use the previous results to check the validity of the harmonic oscillator model and the equipartition theorem at the equation (1.5). There is a relation which connects the maximum of the voltage power spectral density with the maximum of the amplitude power spectral density, it is here below reported from the article Belacel et al., 2017.

$$S_{zz}(f_0) = \frac{2k_B T Q}{(m_{eff}(2\pi f_0)^3)} \tag{2.4}$$

Equation (2.4) gives the expression of the maximum value assumed by the amplitude power spectral density, which is at f_0. What we need to do, it is to relate the maximum of the voltage power spectrum obtained experimentally with its correspondent maximum value of amplitude power spectral density. For example, considering the case of the out-of-plane mode in vacuum, the correspondent value is $S_{zz}(f_0) = 0.2548\ (pm)^2/Hz$, this is obtained considering $T = 293\,K$, the quality factor Q and the eigenfrequency f_0 extracted by the fit and the effective mass $m_{eff} = 6.7\,pg$. Then considering the figure 2.2, the noise floor is subtracted to the fit and the Lorentzian curve extracted is normalized to be $0.2548\ (pm)^2/Hz$ at the frequency $f = f_0$, the result of the processing is shown in figure 2.3.

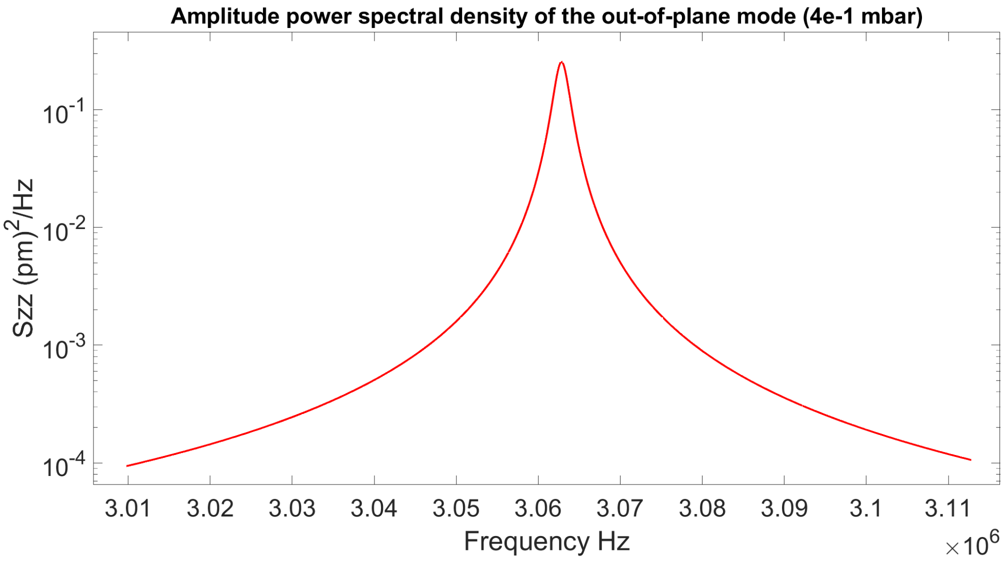

Figure 2.3: Amplitude power spectral density of the out-of-plane mode in vacuum. Result obtained from the correspondent plot of the voltage power spectral amplitude in figure 2.2. The y-axis is visualized in logaritmic scale.

It is very interesting to underscore that this procedure enables the determination of which will be the maximum amplitude of oscillation of the bridge independently from where the laser is hitting the sample. Said in other words, it is good to try to detect the thermal noise hitting the sample in the middle because the Lorentzian curve comes out better from the noise floor and this provides better characterization. Anyway the equation (2.4) always gives theoretically the correspondent maximum possible amplitude of the oscillator, indeed the effective mass m_{eff} is calibrated to represent the bridge in the middle.

Coming to the equipartition theorem, it is easy now to check that the area under the curve in figure 2.3 is half of the variance of the amplitude of oscillation of the bridge, the same of the equation (1.4). This is a crucial point, because the integral (1.4) is from $-\infty$ to $+\infty$, instead in figure 2.3 it is only taken into account the positive part of the axis of the frequencies. In the negative semi-axis of the frequencies there is an exact equal replica of the Lorentzian curve existing for positive values of frequencies, so to get the variance of the amplitude, the area under the Lorentzian in figure 2.3 must be multiplied by a factor 2.

Moreover from the equipartition theorem relation (1.5), the variance of the amplitude turns out to be $\langle z_{eq}^2 \rangle = \frac{k_B T}{m_{eff}\Omega_0^2}$, in which Ω_0 is the experimental found eigenmode. Calling A the area under the curve in the positive semi-axis of the frequencies, the Wiener-Khinchin theorem variance is

$\langle z^2_{WK} \rangle = 2A$. In the following table there is the comparison between $\langle z^2_{WK} \rangle$ and $\langle z^2_{eq} \rangle$ which should match:

Theorem	Variance
Wiener-Khinchin	$1609.8\ (pm)^2$
Equipartition	$1630.3\ (pm)^2$

Table 2.2: Comparison between the variance of the amplitude of oscillation of the bridge found with the Wiener-Khinchin theorem (1.4) and the equipartition theorem (1.5).

In the end, it is useful to calculate now the relation between voltage output of the balanced photodiode and picometers of displacement, it is just necessary to take the ratio between the peak of the out-of-plane mode expressed in amplitude in figure 2.3 and the peak of the same mode in figure 2.2 after subtracting to it the noise floor for coherence, notice that both figure refer to the vacuum acquisition but the ratio must be independent of the pressure conditions. The described calculation gives a number in $(pm)^2/V^2$ from which taking the square root leads to a responsivity $R \sim 5.31 \cdot 10^4\ pm/V$, this formula says that any quantity measured in volt from the setup must be multiplied by $5.31 \cdot 10^4 pm/V$ to get the corresponding amplitude of oscillation of the bridge in picometers.

Ring-down method (Oscillation damping)

The second method used to characterize the sample is the ring-down method, which consists in strongly excite the motion of the bridge and then measure the oscillation damping. An external mechanical force is applied by the electrodes and after the excitation the oscillator vibrates dissipating all the received energy. Considering the setup in figure 1.3, now the oscilloscope doesn't have in input the two DC signals from the diodes, but instead it has the differential output of the balanced diode which before was going into the spectrum analyser. In the meanwhile a signal generator in used to apply a pulse signal to the sample, and it is synchronized with the oscilloscope in order to visualize the effect of the oscillation of the sample.

As anticipated in the introduction, the electrodes generate an electric field which is represented by the blue lines in figure 1.1 and this electric field creates a dipole in the bridge. In addition the electric field all around the sample is not homogeneous and in a perfectly symmetric structure it gives a non-zero force along the out-of-plane direction (z-axis), because a dipole immersed in an electric field gradient is forced to move toward the gradient of the field.

This technical explication is necessary to understand why when a voltage signal is applied to the electrodes the main stimulated eigenfrequency is expected to be the out-of-plane one, since the force is almost fully pointing in z-axis.

As matter of fact the ring down method of this section serves as a further investigation of the

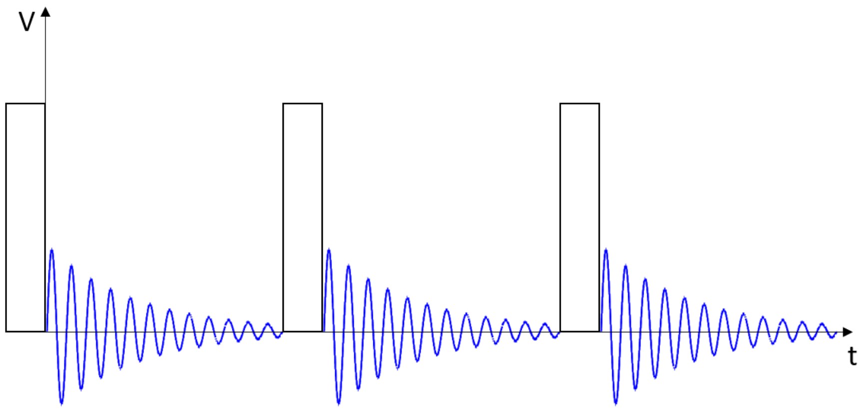

Figure 2.4: In black the pulses delivered by the signal generator to the bridge and in blue the oscillation damping that is visualized on the oscilloscope. Notice that the frequency of application of the pulses must be low enough to let the stimulated oscillation be damped, in such a way that it can be fitted. The x-axis is time and the y-axis is voltage, the amplitudes of the signals and the time intervals are not in scale for the sake of clarity of the image, in the next part of the discussion are given the real orders of magnitude.

highest quality factor of the oscillator, which is of main interest to induce controlled amount of strain into the semiconductor. In figure 2.4 is given a temporal scheme which shows the external stimulation and the consequent response of the bridge during the ring-down technique, the signal generator is set to generate a pulse with very low frequency compared to the oscillation frequency of the out-of-plane mode and with a very small duty cycle, this is to be able to visualize on the oscilloscope the oscillation damping of the bridge after the excitation, before the new pulse will be delivered to the sample.

The oscilloscope in this application of the setup, plots the Brownian motion of the bridge when no external voltage is applied, then after the first pulse of the signal generator the bridge is strongly pushed in the out-of-plane axis and dissipates the absorbed energy up to coming back to just being perturbed by the thermal noise. The reason for which the quality factor can be estimated through this procedure relies on the definition of quality factor, indeed the envelope of the oscillation of the bridge decays exponentially with a time constant τ which is connected to the quality factor by the following relation:

$$\tau = \frac{2Q}{\omega_n} \tag{2.5}$$

In this formula ω_n is the eigenmode of the oscillator, in the case under study it coincides with the angular frequency of the first out-of-plane mode Ω_0. At higher quality factor corresponds higher time constant of the envelope of the oscillation, so it implies that oscillators with higher quality factor keep for a longer time the energy initially given to them.

The method is applied first at ambient pressure and then in vacuum, a pulse of amplitude 10 V, frequency 1000 KHz and 0.083% of duty cycle is sent to the bridge, the acquisitions taken by the oscilloscope are reported in figure 2.5.

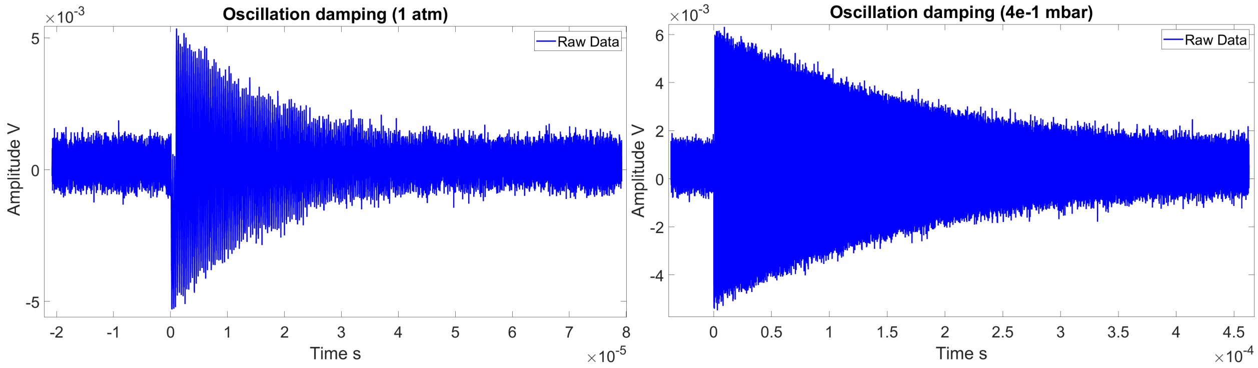

Figure 2.5: Oscillation damping acquired with the oscilloscope at ambient pressure (1 atm) and in vacuum ($4.1 \cdot 10^{-1} mbar$). Notice that in vacuum the oscillation damping is much slower as the quality factor increases, see equation 2.5.

Before going to the result it is interesting to show the first oscillations registered after the pulse at time t = 0 s. With the purpose of reducing the noise of the acquisition, the raw data are smoothed to have a better view of the oscillations and enable a more reliable extraction of the peaks later, the same procedure is applied in both pressure conditions. In figure 2.6 are shown the first oscillations after the pulse at t = 0 s at ambient pressure.

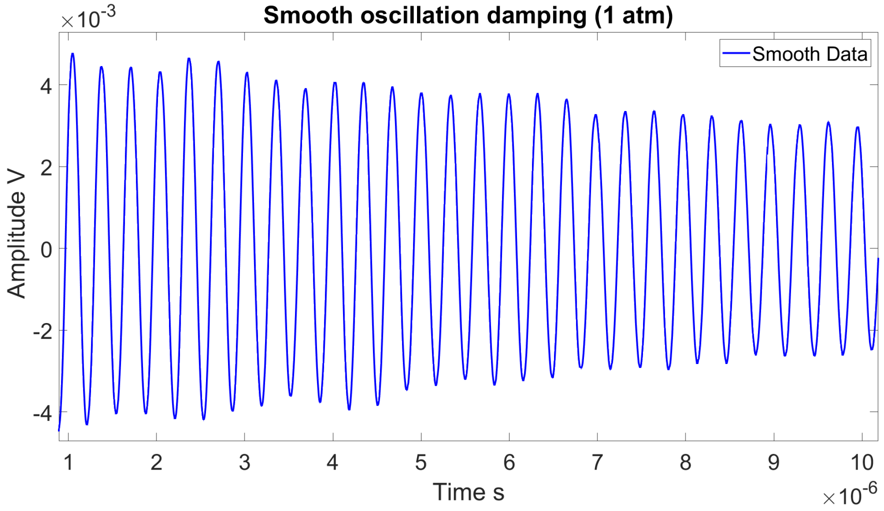

Figure 2.6: Oscillation damping at ambient pressure after the smoothing of the data.

It is evident from figure 2.6 that there is also a non-zero contribution of the in-plane mode to the oscillation, because the envelope is not homogeneously decreasing, so it means it contains a sum of two sinusoidal functions, one with the in-plane mode frequency and the other with the out-of-plane mode frequency. The predominance of the out-of-plane one will be checked after by the Fourier transform of the signal.

Coming back to the quality factor estimation, the envelopes of the up part of the oscillations in figure 2.5 are extracted and after the smoothing are fitted with an exponential, the fits are plotted in figure 2.7.
It is highlighted that in the vacuum acquisition there are many more points and this increases the necessity of a smoothing of the data to reduce the noise due to oversampling. Nevertheless this condition due to not perfect experimental operation is not a big problem because the data analysis still leads to a satisfying fit of the envelope.

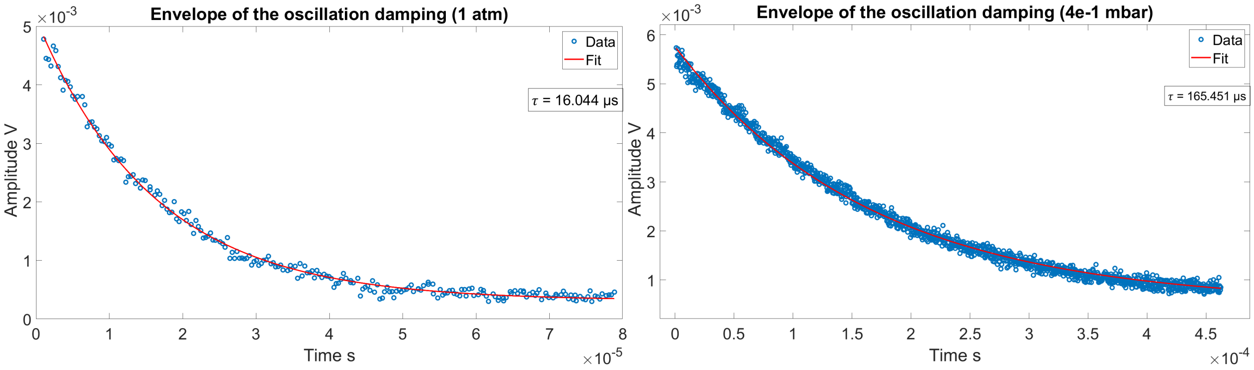

Figure 2.7: Fit of the oscillation damping acquired with the oscilloscope at ambient pressure (1 atm) and in vacuum ($4.1 \cdot 10^{-1} mbar$). The blue empty dots are peaks of the smoothed data, while the red line is the exponential fit, in the upper right there is the value of τ obtained.

Once τ is derived the correspondent quality factor it is simply calculated by inverting the formula (2.5). Anyway in order to be consistent and well compare the ring down method with the spectrum analyser method, the eignemode Ω_0 is now extracted by the Fourier spectrum of the oscillations observed in the oscilloscope. The Fourier transform of the oscillations damping in figure 2.5 are performed and showed in figure 2.8.
The Fourier analysis proves that the oscillator is mainly vibrating with the frequency of the out-of-plane mode and again due to the larger amount of points the reconstruction is more noisy and detailed in the vacuum case. Finally in the table 2.3 are summed up the two values of Ω_0 extracted by the Fourier transform and the correspondent quality factors.
The final outcome gives eigenfrequencies and quality factors which are in good agreement with the ones found with the spectrum analyser method, see table 2.1.

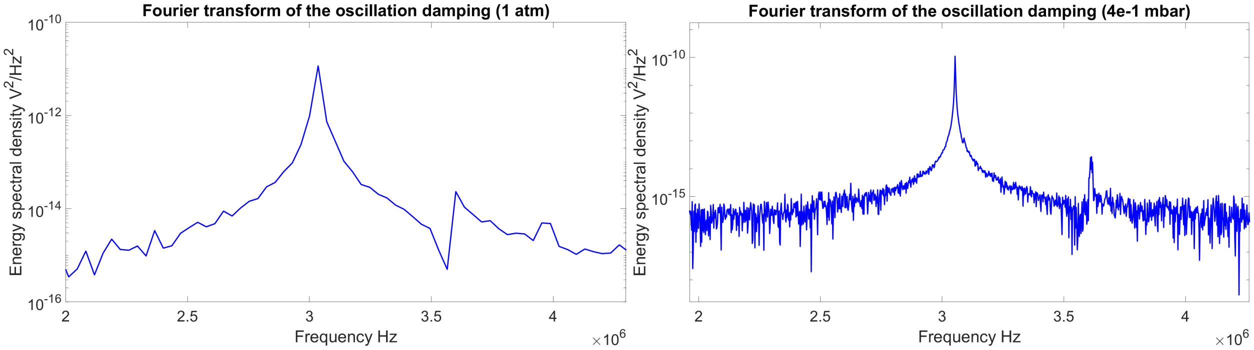

Figure 2.8: Fourier transform of the oscillation damping acquired with the oscilloscope at ambient pressure (1 atm) and in vacuum ($4.1 \cdot 10^{-1} mbar$). On the y-axis the energy spectral density of the signal is showed in logaritmic scale.

Pressure	Eigenfrequency	Quality factor
1 atm	3.0358 MHz	153
$4.1 \cdot 10^{(-1)} mbar$	3.0535 MHz	1587

Table 2.3: Eigenmodes and quality factors found with the Fourier transform analysis of the oscillation damping both at ambient pressure and in vacuum.

Driving force

The reason for which it is believed that the mode at $3\,MHz$ is the out-of-plane mode is exactly the result evidenced by the ring-down method of evaluation of the quality factor, because it is clear that pushing the bridge with the driving voltage puts in motion mainly the $3\,MHz$ mode. Since the driving is expected to be only in the z-axis for a perfect structure, it means that the assumption that has been made at the beginning of this work is correct. Nevertheless in precedent research projects still remained a doubt about this point, because due to not perfectly symmetric distances of the electrodes from the bridge, there could be a non zero force in the x-axis which could actuate more the in-plane mode that the out-of-plane mode. In order to eliminate this possibility of redistribution of the forces, it is presented here an estimation of the components of the force on x-axis and z-axis, which is based on theory and experimental observation. The sample under use has been analyzed in the SEM to check its dimensions, in particular the relative distances between the electrodes and the bridge. Moreover it is taken the chance to check the length and the width of the sample, which are approximately as expected $w = 250\,nm$ and $l = 17\,\mu m$. In figure 2.9 is shown a top image of the bridge in which its length is measured and an image of a zoom from the top which shows that actually is true that is present a quite large asymmetry of the distances between the bridge and the electrodes, these relative distances on the x-axis are around $670\,nm$ and $925\,nm$.

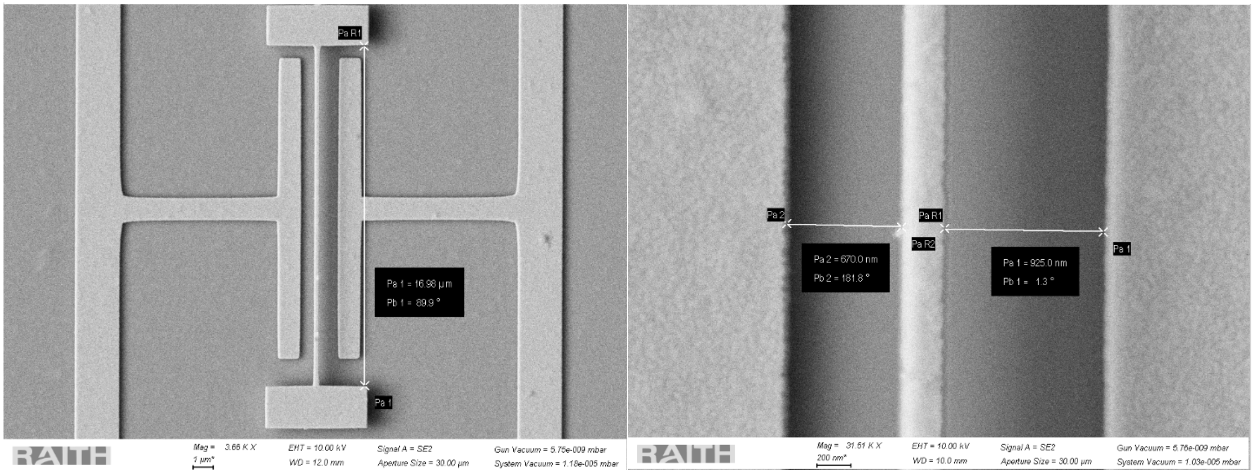

Figure 2.9: SEM images of the bridge from the top, it is measured the length which is matching the fabrication parameter $l = 17\,\mu m$ and the distances between the bridge and the electrodes which are about $670\,nm$ and $925\,nm$.

The model which is implemented to measure the components of the force acting on the bridge relies on the assumption that the electrodes can be treated as infinite charged wires when a voltage drive is applied to them, this means that the corresponding electric field generated by each of the electrodes in a point in the vacuum space is though as follows:

$$\vec{E} = \frac{\lambda}{2\pi\epsilon_0 r} \cdot \vec{u_r} \tag{2.6}$$

In equation (2.6) λ is the charge per unit length, ϵ_0 is the vacuum dielectric constant, r is the distance between the electrode and the point under consideration and $\vec{u_r}$ is the versor of the vector going from the wire toward the point in the space in which the field is evaluated.

By the way, it is true that the bridge has a finite size, therefore to treat it as a unique body under the electric field, multiple geometrical considerations are implemented following the top scheme in figure 2.10.

It is considered that the x-distance from the first electrode is around $670 + 125\,nm$ and from the second electrode is $925 + 125\,nm$, in this way is taken a point at half of the width of the bridge which is $w = 250\,nm$. Then the distance on the z-axis must be taken into account, the bridge is suspended with a height of $500\,nm$ which is the thickness of the AlGaAs sacrifacial layer, see 1.1. At this value must be subtracted roughly around $150\,nm$ of thickness of the electrode which is closer to the bridge, but at the same time it is summed around $200\,nm$ to take a point which is between the GaAs and Au layers, this choice is arbitrary but hopefully not too far from the center of mass of the bridge, the result is a z-distance for both the electrodes of about $550\,nm$. This geometrical evaluation is necessary to well set the calculation of the electric field acting on the bridge, especially taking a point roughly in the middle is a way to try to express as much as possible a more reliable result of the resulting force. Basically the problem is simplified treating the bridge as made of a unique material with the same polarizability at which the electric field coming from the two electrodes is applied in the center of mass. Naturally, being the bridge made of two different materials, the chosen height of the center of mass is only approximated, in fact the force and the electric field components will be evaluated in a range of possible effective height values, in such a way to check if there is any remarkable difference.

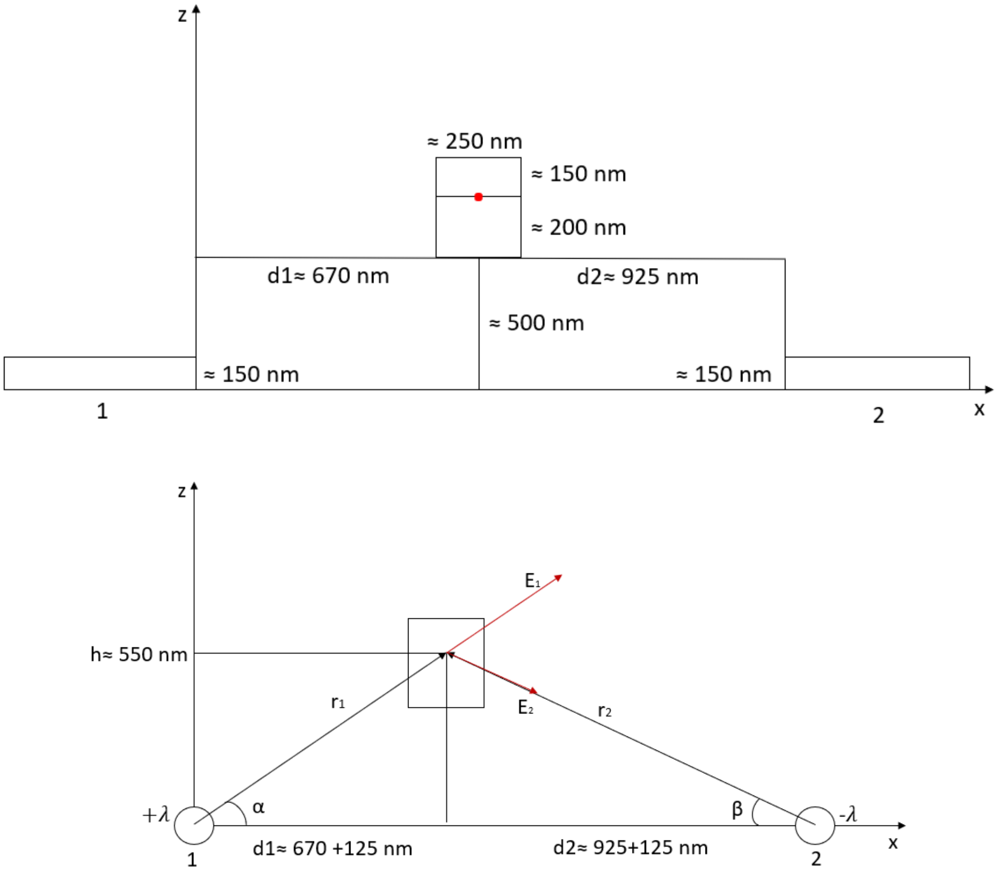

Figure 2.10: The top image is a scheme of the sample geometry in x-z cross section, the red dot indicates the arbitrary point taken to calculate the force acting on the bridge. The thickness of both the lateral electrodes 1 and 2 is estimated to be about 150 *nm*. The thickness of GaAs and Au is respectively 200 *nm* and 150 *nm*, while the width is 250 *nm*, d1 and d2 are the distances between the extremes of the electrodes and the bridge, finally 500 *nm* is the thickness of the removed AlGaAs sacrificial layer.
The bottom image is the final simplified scheme used to implement the calculation, the empty circles are the electrodes considered now dimensionless, the rectangle is the bridge, r_1 and r_2 are the moduli of the vectors pointing from the electrodes to the chosen point of the bridge, E_1 and E_2 are the electric fields applied on the bridge considering the electrode 1 positively charged and the electrode 2 negatively charged.

In the bottom image in figure 2.10 is given the simplified scheme used to solve the problem, it represents just one instant in which an RF voltage is applied to the electrodes, but any other instant in which the charge of the electrodes is less or the sign is reversed is completely equivalent for the determination of the ratio of the components of the force $\frac{F_z}{F_x}$. From the chosen scheme it is possible to write the Ex and Ez components of the field acting on the bridge apart from fundamental constants:

$$\begin{aligned} Ex &\propto \frac{cos(\alpha)}{r1} + \frac{cos(\beta)}{r2} \\ Ez &\propto \frac{sin(\alpha)}{r1} - \frac{sin(\beta)}{r2} \end{aligned} \tag{2.7}$$

Moreover the electric force acting on the bridge is given by the relation (Landau and Lifshitz, 1984):

$$\vec{F} = (\vec{p} \cdot grad)\vec{E} \tag{2.8}$$

In this equation $\vec{E}$ is the total electric field acting on the bridge and $\vec{p}$ is the total electric dipole induced by the field itself which is proportional to the field $(\vec{p} \propto \vec{E})$. The proportionality constant is the same for both p_x and p_z components because the bridge is considered as made of a unique hybrid material, so the x and z components of the force can be extracted:

$$\begin{aligned} Fx &\propto (E_x\frac{d}{dx} + E_z\frac{d}{dz})E_x \\ Fz &\propto (E_x\frac{d}{dx} + E_z\frac{d}{dz})E_z \end{aligned} \tag{2.9}$$

The components of the force are calculated together with the electric field components and are both plotted as function of the height h of the chosen point in the bridge, in such a way to see how the height influences the ratio $\frac{F_z}{F_x}$, see figure 2.11.

The behaviour of the F_z component is coincident with the one obtained in the reference article (Unterreithmeier, Weig, and Kotthaus, 2009) and the electric field is prevalent on the x-axis since the Ez component tend to be canceled by the two opposite contribution of the electrodes, in a perfectly symmetric structure Ez would be zero for any value of the height. Given our asymmetry condition on the x-axis, from the performed calculation it is evident that in absolute value Fz is always larger than Fx apart from the case in which the height is very small (below 100 nm), for the value of $h = 550\,nm$ the ratio is $\frac{Fz}{Fx} \sim 9.5$. To be precise, inside the range of height $h = [350, 700]\,nm$, the ratio $\frac{Fz}{Fx}$ has a minimum value of ~ 3.8, since $350\,nm$ and $700\,nm$ are respectively the smallest and

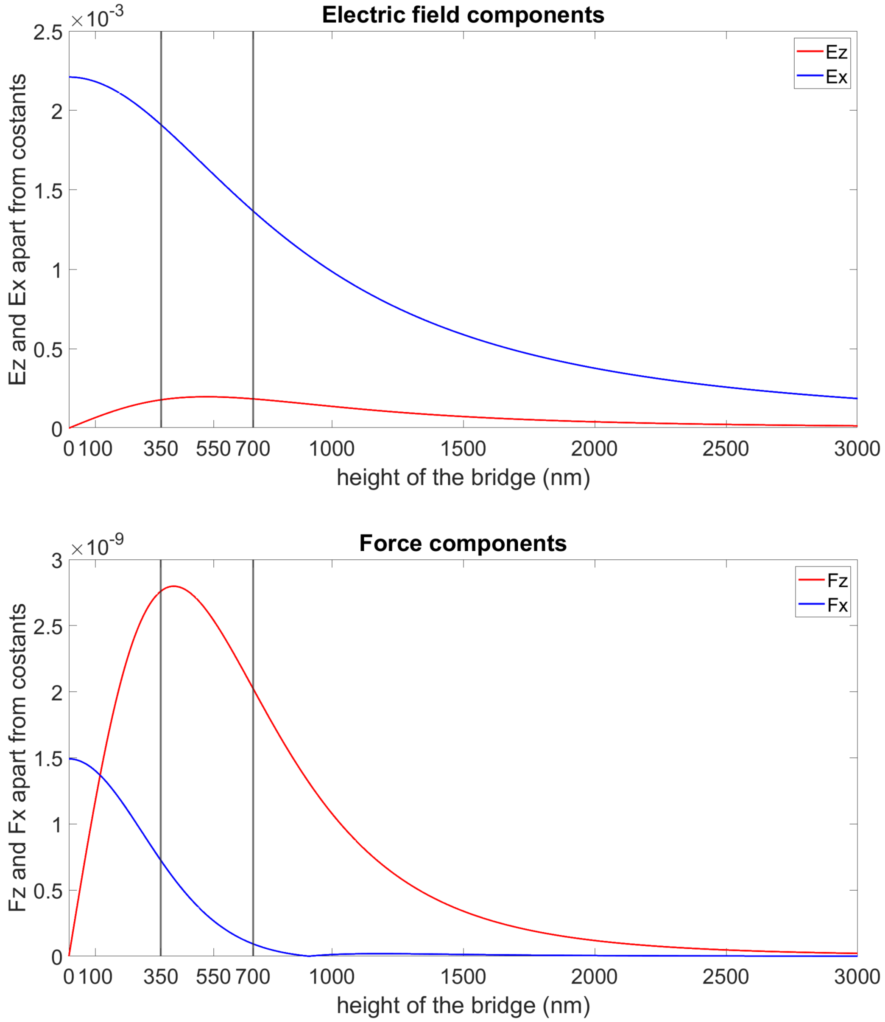

Figure 2.11: Ex and Ez are in arbitrary values as expressed in equation (2.7). Fx and Fz are in arbitrary values, calculated as the absolute value of the expressions (2.9), Fx presents a corner point before 1000 nm of height which manifests an inversion of the sign of the Fx force direction that could be further investigated. In both images are shown the boundaries of the interval $h = [350, 700]nm$, where 350 nm and 700 nm are respectively the smallest and the largest z-distance of the bridge from the electrodes.

the largest z-distance of the bridge from the electrodes, this states unequivocally that Fz is much larger than Fx for all the possible z-coordinates of the chosen point in the bridge.

Finally can be concluded that F_z is dominant with respect to F_x, because not only F_z is larger than F_x but also as found with the Fourier transform of the ring-down oscillation, the main contribution comes from only one of the two modes, the one at 3 MHz. The conclusion is that even though the asymmetry of the sample the driving force is mainly on the z-axis and therefore the 3 MHz mode must be the out-of-plane mode as assumed at the beginning.

2.2 Non-linear limit

The final part of the characterization consists on estimating which is the voltage amplitude of sinusoidal signal that can be applied to the electrodes such to drive the bridge to reach the saturation of its amplitude of vibration. For higher amplitude of vibration, the induced strain in the semiconductor will be also higher, so this measurement is necessary to set the boundaries of operation of a future device exploiting this concept.

For a technical reason the data of this section are taken from a previous measurement carried out by the postdoctoral student Jiawen Liu. The measure has been done on the exact same kind of sample that has been characterized in the first part of this chapter up to now. Anyway slightly different eigenfrequencies and quality factors can be due to the fabrication variability but do not affect the proof of concept which is the goal of this work.

The name of this section refers to the fact after a certain threshold voltage applied to a mechanical oscillator, the equation of motion of the corresponding harmonic oscillator changes because of the influence of the non-linear cubic term of the amplitude which starts to play a role, the equation which describes this condition is the Duffing equation (Nayfeh and Mook, 1995).

The non-linear regime is tested via the use of a lock-in instrument which sends to the sample an RF signal $V_{RF} = V_p \cdot \sin(\omega t)$, the instrument sweeps the frequency of the signal in a range containing the two modes of the bridge. At the same time the lock-in receives in input the differential output of the balanced diode and displays it in volt as function of the frequency of the signal applied in output. In figure 2.12 is plotted the answer of the bridge to a sinusoidal RF drive with four different maximum amplitude values, at pressure between 0.1 and 1 mbar.

In this work are not discussed the characteristics of the Duffing non-linearities, what is of interest for the project aim is to have an estimation of the saturation amplitude of the oscillator. In fact at certain amplitudes of the RF signal applied, the response of the bridge is not drastically increasing anymore, in the present case at voltage amplitude $V_p = 4V$ there is already a pretty good saturation, see figure 2.12. In order to be coherent, for each set of measurements we should retrieve a new picometeres-voltage relation pertinent to the specific sample and setup alignment, but once the detection system is close to the optimum the differences are small and not relevant for this proof of concept.

Let's take under consideration the maximum of amplitude obtained with $V_p = 4V$ and use the ratio $R \sim 5.31 \cdot 10^4\, pm/V$ to convert the top value of the purple curve from volt to picometers, the result is that for an RF signal at frequency 3.075 MHz the out-of-plane mode oscillates with a maximum displacement $z_{max} \sim 48.2\, nm$. The Duffing regime is characterized by a huge drop in the amplitude of oscillation which occurs after a threshold voltage, as a consequence for practical application the frequency of the drive must be well set not to overcome this value, in the case under study the frequency must be not higher than 3.075 MHz.

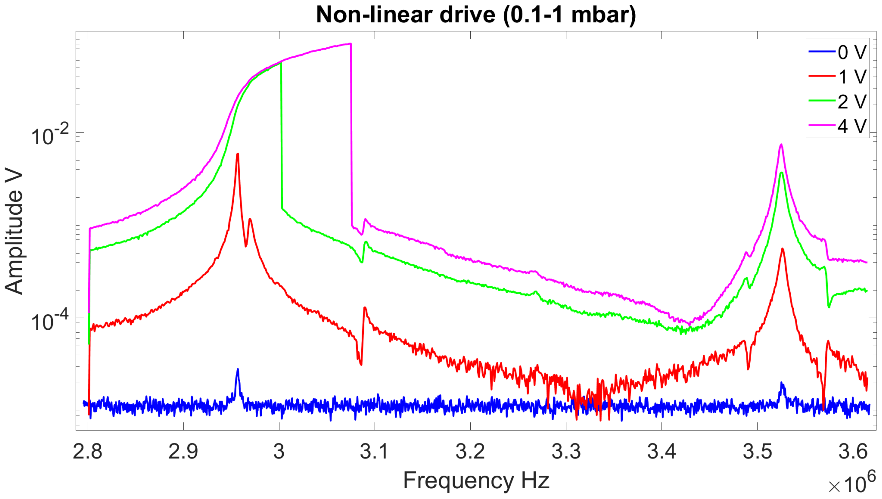

Figure 2.12: Amplitude of oscillation of the bridge as function of the driving signal frequency applied by the lock-in instrument in vacuum (between 0.1 and 1 mbar). Scans at increasing amplitude V_p are run to see the arise of the non-linear regime of the oscillator, the blue signal is just the Brownian motion since the amplitude of the signal is zero. The red curve at $V_p = 1V$ is still a linear response of the oscillator, which becomes effected by non-linearities only for the others curves at $V_p = 2V$ and $V_p = 4V$.

Finally, it is showed that from the data in figure 2.12 it is possible to give an estimation of the ratio of the driving components of force which are applied to the modes of the bridge. For pressure between (0.1-1 mbar), the quality factors of the out-of-plane and in-plane mode have been found to be about $Q = 1200$ and $Q = 600$ respectively and the corresponding eigenfrequecies are 2.95 MHz and 3.53 MHz. Once the angular eigenfrequencies Ω_0 are known, the effective stiffness can be calculated as $k_{eff} = m_{eff} \cdot \Omega_0^2$ and given the maximum of amplitude z_{max} in picometers at angular frequency Ω_0 is straightforward to get the force that the electrodes express through the formula:

$$F = \frac{z_{max} \cdot k_{eff}}{Q} \tag{2.10}$$

Equation 2.10 is valide in the linear regime, so it is taken under consideration the red curve ($V_p = 1V$), extracting the maximum at 2.95 MHz and at 3.53 MHz it is found that the forces that push the out-of-plane and in-plane mode are $F_{out} \sim 0.6056\, pN$ and $F_{in} \sim 0.1648\, pN$ while their ratio is $\frac{F_{out}}{F_{in}} \sim 3.68$ which is a value of the same order of magnitude of the one found with the driving force scheme in chapter 2.

Chapter 3

STRAIN ENGINEERING

In the last chapter is given a proof of concept calculation that estimates the amount of strain reachable in the bridge, which implies a change in the bandstructure of GaAs and sets the connection between classical and quantum phenomena for future quantum devices applications.

3.1 Driven strain

At the end of the second chapter it has been found that applying an RF sinusoidal signal with $V_p = 4V$ to the bridge, the out-of-plane mode reaches a maximum displacement of about $48.2\,nm$ at frequency $3.075\,MHz$. In order to calculate the stress induced inside the material it is used the following relation from beam mechanics (Senturia, 2001):

$$\sigma(d,x) = \frac{E \cdot d}{\rho(x)} \tag{3.1}$$

In this equation sigma is the stress measured in pascal, E is the Young's modulus of the bridge taken as average between the GaAs and Au Young's moduli as already done for the density, meanwhile $\rho(x)$ in this context refers to the radius of curvature of the bridge and d is the distance from the zero curvature plane (neutral plane) of the beam to the point in which the stress in evaluated along the radius of curvature axis. In our case the average elastic modulus is considered to be $E \sim 82.7\,GPa$ and the neutral axis is taken in the middle of the thickness of the bridge even if the GaAs and Au have different density and different thickness the result is not changing significantly, so the maximum value of d is the thickness of the bridge divided by two $\mu/2 = 175\,nm$.

In addition must be said that in the formula (3.1) the sign is not evidenced for simplicity, in reality it is conteined inside the definition of strain, which is $\epsilon = \frac{d}{\rho(x)}$. The strain is positive or negative depending on which of the sides of the beam divided by the neutral plane is considered, in the side where there is compression ϵ is negative, meanwhile in the side where there is extension ϵ is positive.

Furthermore for small displacements the radius of curvature is related to the amplitude of displacement of the beam through the equation (Senturia, 2001):

$$\frac{1}{\rho(x)} = \frac{d^2Y(x)}{d^2x} \tag{3.2}$$

$Y(x)$ is the amplitude of the displacement and x is the position along the length of the beam, the analytical expression of $Y(x)$ is normalized in such a way that $Y(L/2) = z_{max}$ and that $Y(0) = Y(L) = 0$, where L is the bridge length. In this way, the experimental results of the driven oscillation can be combined with the theoretical expression of the amplitude $Y(x)$:

$$Y(x) = a \cdot [(\cosh(\beta x) - \cos(\beta x)) - \frac{\sinh(\beta L) + \sin(\beta L)}{\cosh(\beta L) - \cos(\beta L)} \cdot (\sinh(\beta x) - \sin(\beta x))] \tag{3.3}$$

In the equation (3.3) a stands for the normalization constant which is chosen such that $Y(L/2) = 48.2\,nm$ and β is the constant that for the fundamental mode respects the relation $\beta \cdot L = 4.73004$. Substituting equation (3.2) into equation (3.1) it is found:

$$\sigma(\mu/2, x) = \frac{E \cdot \mu}{2} \frac{d^2 Y(x)}{d^2 x} \tag{3.4}$$

Finally in figure 3.1 are plotted both the amplitude $Y(x)$ and the stress $\sigma(\mu/2, x)$ described by equations (3.3) and (3.4). In particular the plot of the stress refers to the lower side of the bridge, in fact the strain is negative at the center of the beam (compression) and than changes sign becoming positive (extension) close to the anchoring points, on the other side of the bridge the strain and the stress are simply opposite in sign.

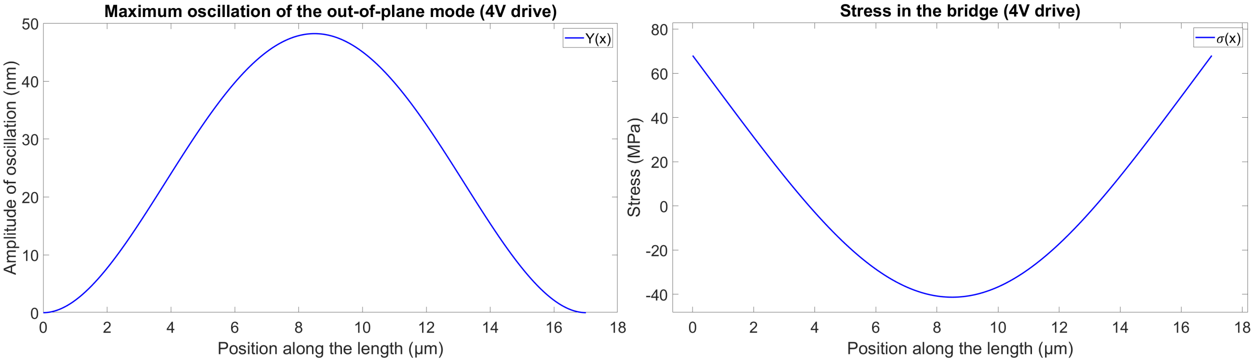

Figure 3.1: On the left the maximum amplitude of oscillation reachable with the out-of-plane mode when an RF sinusoidal signal of frequency 3.075 MHz and $V_p = 4V$ is applied to the driving electrodes, the peak at half of the length is normalized to be 48.2 nm. On the right the corresponding stress distribution, the maximum value of about 68 MPa is achieved at the extremes of the bridge. The stress values must be considered in magnitude, its sign is just due to sign of the strain.

The maximum value of stress of about 68 MPa is reached at the beginning of the anchoring pillars, which compared to the Young's modulus of the bridge $E \sim 82.7\,GPa$ gives a maximum strain $\epsilon = \frac{68\,MPa}{82.7\,GPa} = 0.0822\,\%$, this number is close to the 0.1% strain value that has been obtained in another related work in progress research project of the QUAD group.

In the end it is underscored that for $Y(x)$ and its corresponding second derivative $\frac{d^2Y(x)}{d^2x}$ are taken under consideration the expressions which are valid for a linear oscillator, meanwhile the limit of $48.2\,nm$ it is reached when the bridge is driven up to the Duffing regime. Nevertheless, the non linear correction of the radius of curvature is dependent on the first derivative of $Y(x)$ (Senturia, 2001), as a consequence it is expected to be negligible at the extremes due to the fixed anchoring pillars and the highest value of stress is reached exactly there. As a matter of fact, even if theoretically not perfect, the precedent estimation of the maximum obtainable stress it is considered very likely, even though for the purpose of knowing with more accuracy the stress distribution across the length of the bridge, a complete model which includes non-linear effects must be implemented.

3.2 Conclusions

This research project stands as the proof that it is possible to achieve appreciable values of strain in semiconductors driving mechanical oscillators up to their saturation amplitude. The transduction mechanism which is implemented enables large freedom of integration and low power consumption in a broad range of future optoelectronics applications, in particular the possibility to tune semiconductor laser emission upon controllable modification of the bandstructure. The next step will be try to engineer the reachable strain by optimizing the oscillator structure dependently on the desired application. In particular, since possible application may involve quantum structures along the entire oscillator, it would be interesting to analyze in detail with simulations the strain distribution in all the chosen structure rather than just at the extremes. For the future optimization of the achievable strain in driven optomechanical oscillators, it would be necessary to put together further theoretical considerations with the awareness of the limits of available fabrication and the limit voltage applicable before the breaking point of the device. From equation (3.4) it is easy to see that for a thicker beam the strain will increase, but at the same time after a certain value of thickness the stiffness will reach an unacceptable higher value and the oscillator will not oscillate anymore at good enough values of amplitude. Therefore a trade of between the thickness of the beam and the amplitude oscillation must be found.

In the end, from what has been investigated up to now, it seams that in next chapter of this research the focus should be on the investigation of the Duffing regime. Indeed the non-linear limit is always going to set the boundaries of this engineering problem, a profound study of its parameters could lead to achieve some gain in the strain induced in the driven oscillators.

BIBLIOGRAPHY

Aspelmeyer, Markus, Tobias J. Kippenberg, and Florian Marquardt (Dec. 2014). “Cavity optomechanics”. In: *Rev. Mod. Phys.* 86 (4), pp. 1391–1452. DOI: `10.1103/RevModPhys.86.1391`. URL: `https://link.aps.org/doi/10.1103/RevModPhys.86.1391`.

Belacel, Cherif et al. (2017). “Optomechanical terahertz detection with single meta-atom resonator”. In: *Nature Communications* 8.1578. DOI: `10.1038/s41467-017-01840-6`. URL: `https://doi.org/10.1038/s41467-017-01840-6`.

Butt, H -J and M Jaschke (Jan. 1995). “Calculation of thermal noise in atomic force microscopy”. In: *Nanotechnology* 6.1, p. 1. DOI: `10.1088/0957-4484/6/1/001`. URL: `https://dx.doi.org/10.1088/0957-4484/6/1/001`.

Calabrese, A. (2019). “Optomechanical terahertz meta-atoms”. PhD thesis. Université de Paris.

Karabacak, D. et al. (May 2006). “Optical knife-edge technique for nanomechanical displacement detection”. In: *Applied Physics Letters* 88.19. 193122. ISSN: 0003-6951. DOI: `10.1063/1.2203513`. eprint: `https://pubs.aip.org/aip/apl/article-pdf/doi/10.1063/1.2203513/14661228/193122\_1\_online.pdf`. URL: `https://doi.org/10.1063/1.2203513`.

Landau, L.D. and E.M. Lifshitz (1984). “CHAPTER II - ELECTROSTATICS OF DIELECTRICS”. In: *Electrodynamics of Continuous Media (Second Edition)*. Ed. by L.D. LANDAU and E.M. LIFSHITZ. Second Edition. Vol. 8. Course of Theoretical Physics. Amsterdam: Pergamon, pp. 34–85. ISBN: 978-0-08-030275-1. DOI: `https://doi.org/10.1016/B978-0-08-030275-1.50008-4`. URL: `https://www.sciencedirect.com/science/article/pii/B9780080302751500084`.

Liu, Jiawen et al. (2022). “Ultrafast Detection of TeraHertz Radiation with Miniaturized Optomechanical Resonator Driven by Dielectric Driving Force”. In: *ACS Photonics* 9.5, pp. 1541–1546. DOI: `10.1021/acsphotonics.2c00227`. eprint: `https://doi.org/10.1021/acsphotonics.2c00227`. URL: `https://doi.org/10.1021/acsphotonics.2c00227`.

Nayfeh, A. H. and D. T. Mook (1995). *Nonlinear oscillations*. John Wiley and Sons.

Senturia, Stephen D. (2001). *Microsystem Design*. Springer US. DOI: `10.1007/b117574`. URL: `https://doi.org/10.1007$%5C%2$Fb117574`.

Unterreithmeier, Quirin P., Eva M. Weig, and Jörg P. Kotthaus (2009). “Universal transduction scheme for nanomechanical systems based on dielectric forces”. In: *Nature* 458. DOI: `10.1038/nature07932`. URL: `https://doi.org/10.1038/nature07932`.